The University Of Sheffield.

This is a repository copy of *Winglet design for vertical axis wind turbines based on a design of experiment and CFD approach*.

White Rose Research Online URL for this paper:
http://eprints.whiterose.ac.uk/146708/

Version: Accepted Version

Article:
Zhang, T.-T., Elsakka, M. orcid.org/0000-0002-4937-8843, Huang, W. et al. (4 more authors) (2019) Winglet design for vertical axis wind turbines based on a design of experiment and CFD approach. Energy Conversion and Management, 195. pp. 712-726. ISSN 0196-8904

https://doi.org/10.1016/j.enconman.2019.05.055

Article available under the terms of the CC-BY-NC-ND licence (https://creativecommons.org/licenses/by-nc-nd/4.0/).

Reuse
This article is distributed under the terms of the Creative Commons Attribution-NonCommercial-NoDerivs (CC BY-NC-ND) licence. This licence only allows you to download this work and share it with others as long as you credit the authors, but you can't change the article in any way or use it commercially. More information and the full terms of the licence here: https://creativecommons.org/licenses/

Takedown
If you consider content in White Rose Research Online to be in breach of UK law, please notify us by emailing eprints@whiterose.ac.uk including the URL of the record and the reason for the withdrawal request.

White Rose university consortium
Universities of Leeds, Sheffield & York

eprints@whiterose.ac.uk
https://eprints.whiterose.ac.uk/

Winglet design for vertical axis wind turbines based on a design of experiment and CFD approach

Tian-tian Zhang[a,b], Mohamed Elsakka[a,c], Wei Huang[b*], Zhen-guo Wang[b], Derek B. Ingham[a], Lin Ma[a], Mohamed Pourkashanian[a]

[a] Energy 2050/Department of Mechanical Engineering, The University of Sheffield, Sheffield, S3 7RD, UK

[b] College of Aerospace Science and Engineering, National University of Defense Technology, Changsha, Hunan 410073, P. R. China

[c] Faculty of Engineering, Port Said University, Egypt

[*] Corresponding author, Email: gladrain2001@163.com.

Abstract

Vertical axis wind turbines (VAWTs) have been attracting an increasing attention in recent years because of their potential for effectively using wind energy. The tip vortices from the VAWT blades have a negative impact on the power efficiency. Since a winglet has been proved to be effective in decreasing the tip vortex in the aerospace field, this paper numerically studies the aerodynamic effect of appending a winglet on the blade of a VAWT. Based on the theoretical motion pattern of the VAWT blade, this paper simplifies the three-dimensional full-scale rotor simulation to a one-blade oscillating problem in order to reduce the computational cost. The full rotor model simulation is also used in validating the result. The numerical approach has been validated by the experimental data that is available in the open literature. Six parameters are applied in defining the configuration of the winglet. The orthogonal experimental design (OED) approach is adopted in this paper to determine the significance of the design parameters that affect the rotor's power coefficient. The OED results show that the twist angle of the winglet is the most significant factor that affects the winglet's performance. A range analysis of the OED results produces an optimal variable arrangement in the current scope, and the winglet's performance in this variable arrangement is compared with the blade without a winglet. For the single blade study, the comparison result shows that the optimal

winglet can decrease the tip vortices and improve the blade's power performance by up to 31% at a tip speed ratio of 2.29. However, for the full VAWT case, the relative enhancement in the power coefficient is about 10.5, 6.7, and 10.0% for TSRs of 1.85, 2.29, and 2.52, respectively. The winglet assists in maintain the pressure difference between the two sides of the blade, thus weakening the tip vortex and improving the aerodynamic efficiency of the surface near the blade tip.

Keywords: VAWT; Winglet design; Orthogonal experimental design; Computational fluid dynamics

1. Introduction

Wind is widely recognized as being a source of clean energy, and it will never be exhausted. Using wind energy to generate electricity, instead of fossil fuels, can not only save the conventional energy resources but also protect the environment [1]. Nowadays, many countries are investigating an increasing amount of funds into establishing wind turbines [2]. Horizontal axis wind turbines (HAWTs) dominate the wind turbine market, and it is effective in large electricity plants. However, the high cost in manufacturing the blades and installing the tall towers limits the use of wind energy. In comparison with HAWTs, the Darrieus type vertical axis wind turbines (VAWTs) are simpler in structure because they can work in any flow direction without the assistance of a yaw control mechanism. Normally, VAWTs have straight blades, which are easier to manufacture than the twisted blades in HAWTs. In addition, the structure of VAWTs make it possible to place the generator and gearbox on the ground and this can reduce the installation and maintenance complexities. All the characteristics in VAWTs can reduce the cost of VAWTs in comparison with HAWTs [2, 3]. In addition, VAWTs are attractive for distributed small scale electricity facilities in urban environments

where there are unstable wind conditions [4], as well as large scale offshore floating turbine for deep-sea installations [5] .

1.1. Current study on VAWTs

The Darrieus type rotor is a lift based VAWT, and it uses blades with airfoil shaped cross sections [6]. The study on Darrieus type VAWTs has many aspects, such as the pitching of the blade, the roughness of the blade surface, the blade thickness, the blade tip speed ratios, etc. Experimental studies on VAWTs are direct and effective. Li et al. [7-12] implemented numerous experiments in a wind tunnel and obtained many valuable results. They concluded that the power coefficient decreases with an increase in the number of blades and that two blades have a higher annual generating capacity in high wind velocity regions [7]. Through change in the pitch angle of the blade, they found that an optimum pitch angle (6°) can effectively improve the power efficiency of their turbine design [11]. In addition, the Reynolds number and solidity of the rotor also affects the performance of the VAWTs [8, 9]. Although wind tunnel experiments are ideal in the study of VAWTs, the expense in building wind tunnels and manufacturing the rotor has limited the development. Also the results show some differences with the field experimental results [10].

The rapid development of computational power makes computational fluid dynamics (CFD) ever increasingly more popular for use in wind turbine aerodynamic design. Numerical simulations of the performance of VAWTs are cheaper and faster than experiments. Therefore, numerous research papers on VAWTs have been published based on CFD analyses. For example, Lanzafame et al. [13] studied the CFD simulation process of VAWTs using the Ansys Fluent software. 2D unsteady CFD models of Darrieus VAWTs using the sliding mesh method is adopted, and the results have been compared with the available experimental data. Based on the CFD approach, Rezaeiha et al. [14] investigated the impact of the operational parameters

(e.g. the tip speed ratio, the Reynolds number and the turbulence intensity) on the performance of VAWTs. Guidelines for the azimuthal increment, domain size and convergence are proposed for the accurate CFD study of the VAWT [15]. Rezaeiha et al. [16] also studied the influence of a fixed pitch angle on the power coefficient of VAWTs. They conclude that a negative pitch angle can improve the power performance of a VAWT, and dynamic pitching might be a more promising approach than fixing the pitching angle. Following Rezaeiha's expectation, Li et al. [17] optimized the blade pitch using a genetic algorithm to maximize the turbine power performance. It is noticed that the optimized pitch angle changes continuously as the rotor rotates and the pitch angle curves differ with different tip speed ratios. Furthermore, in order to determine the optimum airfoil shape for the blades of VAWTs, the VAWTs with the blade airfoils of NACA0018, NACA0021 and NACA0025 have been simulated using a 2D CFD approach by Shukla, et al. [18]. Jafaryar et al. [19] studied the influence of the shape of the airfoil on the performance of VAWTs based on the response surface model and the central composite design technique. The results obtained confirm that the optimum shape of the airfoil is very similar to those obtained using symmetrical blades. In addition to the RANS approach that is normally used in VAWTs simulations, the ALM-LES coupled with the URANS and RANS-LES approaches have been developed in order to obtain more accurate CFD results [20, 21].

The main weakness of a VAWT is its low efficiency in power generation. For this reason, many devices are proposed to enhance the performance of VAWTs. For example, Wong et al. [22, 23] studied the influence of a flat plate deflector, which is placed upstream, on the performance of VAWTs. Due to the flat plate, the free flow accelerated and was deflected by the deflector before impinging on the turbine and thus the rotor's power coefficient is enhanced. Hashem et al. [24] proposed the wind-lens concept which consists of a diffuser

and flanges to collect the wind energy. This mechanism needs yawing devices to ensure that the wind-lens faces towards the wind direction.

1.2. Influence of 3-D effects on the performance of VAWTs

Because of the straight character of the VAWTs blade, most CFD works have simplified the model into a 2 dimensional problem since 2D simulations are easier and faster than 3D simulations. However, 2D simulations often over predict the performance of VAWTs because of the neglect of the vertical flow and the vortices from the trailing edge and the tip end of the blade. Siddiqui et al. [25] investigated the effect of the 3D flow characteristics on the VAWT's simulation results and compared 5 cases in order to study the effect of the tip vortices and the supporting arm. The results obtained show that 2D simulations can over predict the performance by up to 32% in comparison with real time 3D CFD simulations. This result does not only reflect the inaccuracy in the 2D simulations but also illustrates that the efforts in reducing the 3D impact has a promising potential in improving the VAWT's aerodynamic performance.

Among all the 3D effects, the tip vortices have a great impact on the performance of lift-based blades and the scope does not limit to VAWT. Taking the aircraft's wing as an example, the lift is generated because of the pressure difference on the upper and lower surfaces. However, at the tip end of the wing, the high-pressure air is transported from the lower surface upwards to the upper surface, thus causing a reduction in the lift and generating the so-called tip vortex. The flow in the blade's span wise direction caused by the transportation in the blade tip also decreases the efficiency of the wing. The span wise flow on the VAWT's blade is similar to the span wise flow on an aircraft wing. As the VAWT's rotor rotates, both the suction and pressure sides of the blade change their roles continually. This results in more complicated tip vortices than the static wing. Mie-type tip vane and end plate have been proved to be

effective in weakening the tip vortices and enhance the power performance of both HAWTs and VAWTs [26-30]. However, the vane results in increasing the fatigue loading and decreasing the lifetime for the VAWT [31]. Among these devices, the winglet performs better in terms of improving the power coefficient [31, 32]. Although these tip devices have been proposed, more detailed studies are still limited in comparison with the study on the HAWT.

1.3. The novelty in the design of the VAWT's winglet

A winglet is now commonly observed in most of the commercial long range airplanes and this reduces the drag and hence saves fuel [33]. This device helps to isolate the suction and pressure sides of the blade, thus decreasing the tip vortices and improves the blade's performance. During the study of a winglet on an aircraft, the influences of the cant angle, sweep angle, twist angle as well as the winglet direction have been numerically investigated [33-37]. In addition, on using a multi-tipped winglet to decrease the strength of the tip vortices and improve the blade's performance, it has been proved to be an effective way to further enhance the performance of the wing [38]. Inspired by the winglet design in the aeronautic field, engineers are attempting to improve wind turbines' performance in a similar way because these blades also encounter tip vortex problems. For example, Gupta and Amano [39] found that a winglet with a cant angle of 45° performs better than that of the vertical winglet on the blade of the HAWT. Johansen and Sørensen [40] found that the vertical winglet on the blade of the HAWT has an optimal twist angle when all the other parameters are kept constant. Farhan et al. [41] combined the winglet planform with the airfoil design using a CFD approach. The result suggests that a smaller tip length configuration may have a better performance.

However, the flow patterns are very different among the static wing of the aircraft, the blade on the HAWT and the blade on the VAWT. To be more specific, the blade on the HAWT experiences an unevenly distributed incident velocity in the span wise direction and the tip

velocity is the largest. Although the blade of the VAWT has a consistent incident velocity in the span wise direction, the velocity value changes continuously as the blade rotates. In addition, the suction side and the pressure side of the blade of the VAWT convert with each other as the rotation proceeds. This results in time-varying tip vortices in the flow field. As a result, the results obtained from the aircraft winglet design and the HAWT winglet design cannot be applied directly to the winglet design of VAWTs.

Although the wake and tip vortices also have a very strong impact on the VAWT's performance [42], only a few investigations have studied the winglet design for a VAWT. In order to reduce the tip vortices' influence on the efficiency of the VAWT, Rohmann-Shaw [32] performed 3D CFD simulations on a VAWT and investigated the blade tip design. Through a comparison of the end plate and winglet, the author found that the winglet is more effective in improving the aerodynamic efficiency of the VAWT. Tao et al. [43] used the Non-uniform rational basis spline (NURBS) based free form deformation approach in the parametric method in order to design the winglet. This parametric approach assists in the studying of the winglets' configuration more comprehensively [43, 44].

Although previous studies have illustrated that the winglet can improve the aerodynamic performance of the VAWT, they failed to give an optimal approach for the winglet configuration design. It is still not clear which parameters are significant in the winglet design process. This paper defines 6 parameters to parameterize the winglet's configuration [39] and studies their importance in influencing the blade's power coefficient using the orthogonal experimental design (OED) approach [45].

This paper aims to determine the most influential design parameters of the winglet of the VAWT and obtain a good design through the OED approach. Through comparing the aerodynamic performance of VAWTs with and without a winglet, we aim to obtain the

performance enhancement by adding a winglet on the blade tip and determine the working mechanism of the winglet. Section 2 introduces the physical and numerical model that is used in defining the configuration and the flow field of VAWT's blade. Section 3 validates the numerical results obtained using the Ansys Fluent software by comparing the predicted result with the available experimental data. A grid independent analysis is also discussed in this section. In order to reduce the cost involved in the study of 6 parameters, the OED approach is adopted in Section 4. In Section 5, the optimal parameter arrangement in defining the winglet is obtained and its effect on the flow field is studied by comparison with the result obtained for a non-winglet blade. Finally, Section 6 gives the conclusion of this work. The results in this paper show that the twist angle is the most influential parameter in the winglet design for the VAWT. This can help to decrease the complexity and time in the further optimization of the winglet on the VAWT.

2. Physical & numerical model

2.1. Physical model introduction

The NACA 0015 is commonly used as the airfoil for VAWT's blade in the experimental investigations [6]. It is a symmetric airfoil with a good power coefficient performance [24]. Li et al. [12] performed many wind tunnel experiments including using this airfoil and the results are available in the open literature. Based on the work of Li, this paper investigates three-dimensional numerical simulations on a 2-bladed VAWT with a NACA 0015 airfoil for the blades. The chord length (C) of the blade is 0.225m, the height (H) is 1.02m, and because of the symmetric character in the span wise direction, only half the model is studied numerically in this paper. The radius of the rotor (R) is 0.85m and the blade's pitching angle is set to be 6° according to the optimization study of Li et al. [7, 12]. The geometrical features of the rotor is listed in Table 1.

Table 1. The geometrical features of the VAWT model in current work.

Blade profile	Blade number	C (m)	H (m)	R (m)	β (°)	Solidity
NACA 0015	2	0.225	1.02	0.85	6	0.084

Fig. 1 illustrates a schematic of the VAWT's full-model geometry studied in this paper. The freestream wind speed is V_∞ (7m/s) flowing from the left-hand-side across the turbine, with a Reynolds number $Re = 2.89 \times 10^5$, which is typical for the VAWT. It is expected that the results obtained using this turbine will give useful information for VAWTs using other types of airfoils. The operational conditions of the reference rotor in listed in Table 2.

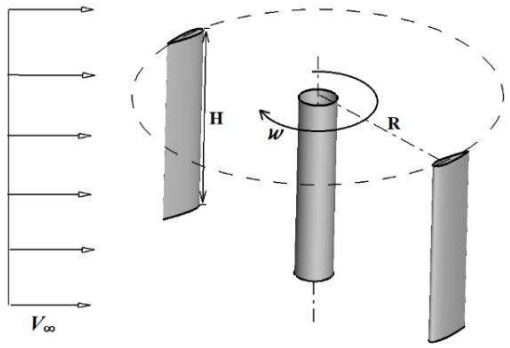

Fig. 1 Schematic of the VAWT geometry employed in this paper.

Table 2. The operational conditions of the VAWT model in current work.

Re	V_∞ (m/s)	ω (rad/s)	TSR
2.89×10^5	7	18.86	2.29

In this paper, the free flow speed is V_∞, the VAWT's rotation speed is ω and the rotor's radius is R. Fig. 2 illustrates the relationships among the velocities and force coefficients in different coordinate systems. V_{real} is the incident velocity of the blade, and it is composed of the free flow velocity V_∞ and the rotation speed ωR. C_l and C_d are the lift and drag coefficients in the velocity coordinate system whose X-axis points to the free flow direction. The azimuthal angle is θ, and the blade's angle of attack is α. C_t and C_n are the tangential and normal force coefficients, respectively, relative to the rotation of the blade. C_x and C_y are the horizontal and vertical force coefficients respectively in the absolute coordinate system that fixed on the shaft.

The tip speed ratio (TSR) defines the ratio between the speed of the blade and the free flow velocity, namely

$$\mathrm{TSR} = \frac{\omega \mathrm{R}}{\mathrm{V}_\infty} \tag{1}$$

According to the sine rule theorem, the relationship between the different velocities is as follows:

$$\frac{\omega \mathrm{R}}{\sin(\theta - \alpha)} = \frac{\mathrm{V}_\infty}{\sin \alpha} \tag{2}$$

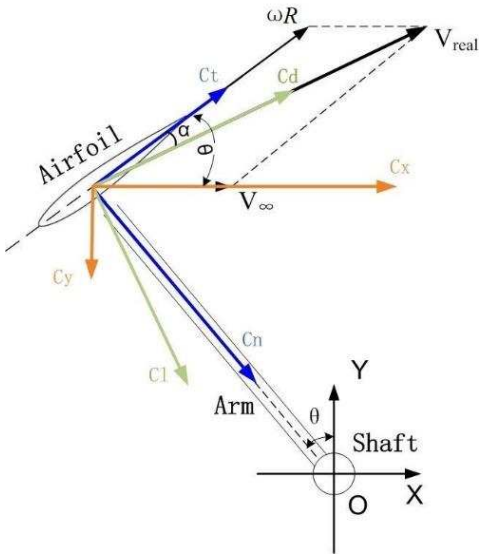

Fig. 2. The relationships among different coordinate systems on the blade of VAWT.

Therefore, the TSR can be calculated as follows:

$$\mathrm{TSR} = \frac{\sin\theta\cos\alpha - \sin\alpha\cos\theta}{\sin\alpha} = \sin\theta\cot\alpha - \cos\theta \tag{3}$$

As a result, the relationship between the azimuthal angle (θ) and the attack angle (α) is given by

$$\alpha = \mathrm{atan}\left(\frac{\sin\theta}{\mathrm{TSR} + \cos\theta}\right) \tag{4}$$

In this paper, an optimal pitch angle β= 6° [11] is adopted so that the VAWT operates in the optimal condition. In this case, the real attack angle of the blade is giving by

$$\alpha = \text{atan}(\frac{\sin\theta}{\text{TSR}+\cos\theta})\text{-}\beta \tag{5}$$

The torque of a single blade and the power of the rotor are calculated as follows:

$$\begin{aligned} \text{Q} &= \frac{\text{R}}{2\pi}\int_0^{2\pi} \text{F}_\text{T}(\theta)\,\text{d}\,\theta \\ \text{P} &= \frac{\text{NR}}{(2\pi/\omega)}\int_0^{2\pi} \text{F}_\text{T}(\theta)\,\text{d}\,\theta = \text{N}\omega\text{Q} \end{aligned} \tag{6}$$

where F_T is the transient tangential force when the azimuthal angle is θ, and N is the number of blades on the VAWT.

The wind turbine performance is normally characterized by its power coefficient (C_P), and the relationship between C_P and the torque coefficient C_Q is given as follows:

$$\begin{aligned} \bar{\text{C}}_\text{T} &= \frac{\frac{1}{2\pi}\int_0^{2\pi} \text{F}_\text{T}(\theta)\,\text{d}\,\theta}{\frac{1}{2}\rho\text{cHU}_0^2} \\ \text{C}_\text{P} &= \frac{\text{Nc}\omega}{2\text{U}_0}\bar{\text{C}}_\text{T} \\ \text{C}_\text{Q} &= \frac{\text{c}}{2\text{R}}\bar{\text{C}}_\text{T} \end{aligned} \tag{7}$$

where c and H are the chord length and height of the rotor, respectively. The tangential force and tangential force coefficient can be obtained directly in the simulations.

When the blades rotate, it is easy to acquire the horizontal and vertical force coefficients namely C_x and C_y. The tangential and normal force coefficients are given as follows:

$$\begin{aligned} \text{Ct} &= \text{Cx}\cos\theta - \text{Cy}\sin\theta \\ \text{Cn} &= \text{Cx}\sin\theta + \text{Cy}\cos\theta \end{aligned} \tag{8}$$

2.2. Modeling strategy

Full size simulations of VAWTs can produce accurate results but the meshing and calculation process can be very time consuming. The grid around the blade, as well as the winglet, occupies a large portion of the total grid number. This can greatly increase the dependence on the computer memory and time. According to the pattern of the motion of the VAWT's blades, the theoretical incident velocity and the attack angle of the blade are functions of the azimuthal angle. Through the relationship shown in Fig. 2, the incident velocity can be calculated, using the cosine theorem, as follows:

$$V_{real} = \sqrt{\omega^2 R^2 + V_\infty^2 + 2\omega R V_\infty \cos\theta} \tag{9}$$

In order to simplify the simulations, we only consider one blade, and we employ a coordinate system that is fixed on the blade of the turbine, and in this relative coordinate system, the blade is performing an oscillating motion around its central axis with an upstream wind speed and angle of attack described by Equations (9) and (5), respectively. Although this motion pattern is different from the full rotor rotation process, the flow conditions for a single blade are similar for both cases. Therefore, without the need to mesh around every blade and winglet, the computation cost can be dramatically reduced, and it is also easier to implement.

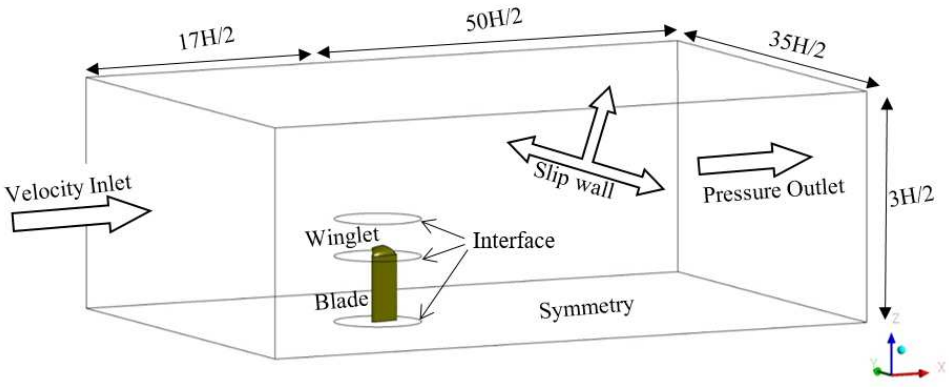

Fig. 3 Schematic of the computational domain for the one blade model (dimensions are not to scale).

Fig. 3 schematically shows the computational domain for the one blade model as employed in this paper. The domain size is defined according to Ma et al. [51]. The blade is rotating around its central axis at a frequency defined according to the rotational speed of the turbine. This is realized by establishing a cylindrical sub-domain around the blade and applying the sliding mesh approach to make this sub-domain rotate. The non-conformal interface boundary condition is used to connect the sub-domain and the stationary flow field domain. Further, a symmetry condition is adopted on the bottom surface so that only half of the whole blade has to be simulated. Also the slip wall condition is used on the side and top of the outfield to avoid the influence of the wall boundary layer on the blade. The velocity inlet condition is employed on the inlet of the flow field domain and the velocity value is calculated by using Equations (9). At the outlet of the flow field, the pressure outlet condition is used.

For a single blade simulation, the incident velocity's direction is always horizontal. Therefore, the dynamic force coefficients obtained in the Ansys Fluent software are the drag and lift force coefficients, namely C_d and C_l. According to the coordinate relationship in Fig. 2, the tangential and normal force coefficients can be acquired using the following formulae:

$$\begin{aligned} Ct &= Cd\cos\alpha - Cl\sin\alpha \\ Cn &= Cd\sin\alpha + Cl\cos\alpha \end{aligned} \tag{10}$$

where α is the angle between the body coordinate system and the velocity coordinate system shown in Fig. 2 and it is normally calculated using Eq. (4). Since the blade has a fixed pitch angle (β) in the current work, α should be calculated using Eq. (5).

Using one blade to simulate the motion of the VAWT saves computational cost but it cannot take the blade-blade interaction and blade-shaft interaction into consideration [52]. The virtual incidence effect is also neglected [53]. These may cause slight inconsistences between the numerical results and the real situation. Nevertheless, it can be used in the primary design

of the blade and the validation using a full-scale rotor simulation is discussed in the following sections. In order to make the design in this work more reliable, a full 3D model simulation of the VAWT will be performed in order to validate the numerical model and verify the efficiency of the final design.

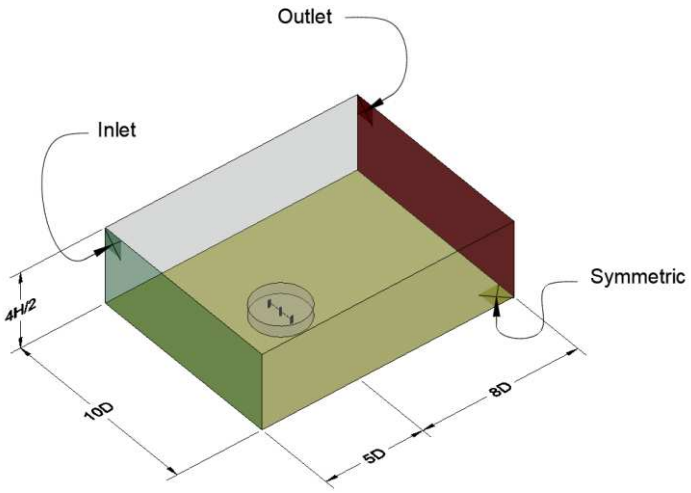

Fig. 4 Schematic of the full 3D model computational domain and the boundary conditions (dimensions are not to scale).

Fig. 4 illustrates the shape of the computational domain and the location of the selected boundary conditions. In this figure, D and H are the diameter and height of the rotor, respectively. The size of this domain is defined according to Elsakka et al. [52]. Due to the symmetrical behaviour of the flow around the blade mid-span plane, only the upper half of the turbine is modelled in order to reduce the computational cost, and this is achieved using a symmetrical boundary condition at the lower surface of the domain. A velocity inlet boundary condition is applied to the upstream end of the domain with a magnitude of 7 m/s to resemble the conditions of the experimental test (Li et al. [12]) while a zero pressure-outlet boundary condition is applied to the downstream end of the domain.

The wind tunnel in Li et al.'s experiment [12] has an open test section. Therefore, the blockage ratio in the experiment is very small. Based on the experiment, we adopted large

domains in our simulation as shown in Fig. 3 and Fig. 4. The blockage ratios for the one blade model and the full rotor model are 0.42% and 2.5%, respectively. Both values are small and comparable with the experimental setup.

2.3. Code Validation & Grid Independency analysis

2.3.1. Grid independency analysis

Fig. 5 shows the structured mesh topologies around a blade and an adjacent arm for the mesh in the full-scale 3D model simulation. The grid is clustered towards the surface of the blade, the winglet and the supporting arms in order to capture the boundary layer more precisely. In order to choose a mesh that is not only precise but also time-saving, three different meshes are used to check the mesh independency. The grid independency analysis is based on the full-scale model shown in Fig. 4. The geometry, as well as the mesh, in the flow field is generated in the workbench in ANSYS 18.2. The domain is discretised using a fully structured shaped mesh, except in the blade tip region and the winglet region, when applicable.

Table 3 shows three different attributes of the meshes. While the number of the nodes around the blade profile changes for the different meshes, the non-dimensional wall distance, y+, is kept constant in order to adhere to the recommended value for the enhanced wall treatment that is used by the transition turbulence model. In these meshes, there are 43 span wise mesh divisions along the blade half-length.

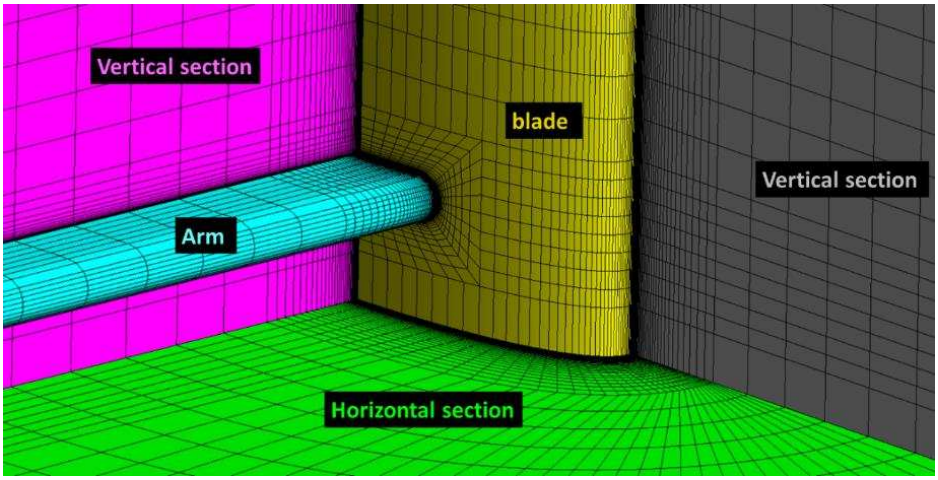

Fig. 5 An illustration of the baseline computational mesh, showing the mesh topologies around a blade and an adjacent arm on different vertical and horizontal sectional planes.

The geometry, as well as the mesh, in the flow field is generated in the workbench in ANSYS 18.2. The domain is discretised using a fully structured shaped mesh, except in the blade tip region and the winglet region, when applicable.

Table 3. The different meshes employed for the three sets of meshes.

Mesh	No. of nodes around the blade 2D profile.	Refinement factor	No. of element	Maximum y+
Coarse mesh	126	0.7	2,146,319	1.2
Baseline mesh	172	1	3,087,970	1.2
Fine mesh	258	1.5	5,141,967	1.2

The flow around the VAWT is modelled using a commercial CFD solver, ANSYS FLUENT [54]. The three-dimensional Reynolds-averaged Naviere-Stokes equations and the transition SST k-ω turbulence model have been utilized in the simulation. The double precision pressure based coupled solver algorithm is utilized in the transient mode and the second-order scheme is used for the spatial and temporal discretization. Using the coupled scheme, a temporal resolution of 540-time steps per cycle is chosen according to Elsakka et al. [52] and this corresponds to an azimuthal increment of 0.67° which slightly coarser than the 0.5 value recommended by Rezaeiha et al. [15] using the SIMPLE scheme. The results are considered at the fifth cycle and this is found to be sufficient to reduce the differences between the results at successive cycles to 0.3% under the current setup using the coupled solver. However, some other studies that utilize the SIMPLE scheme recommend significantly larger number of cycles,

namely between 20–30 turbine cycles. The relative motion between the turbine and the absolute reference frame is modelled using a sliding mesh interface.

The simulations are run on the high performance computer at Sheffield University, and each case employs 32 cores.

Based on these three sets of mesh, the Grid Convergence Index (GCI) [55] is calculated based on the 3D turbine power coefficient by using a safety factor of 1.25 [15]. The GCI_{coarse} and GCI_{fine} are found to be about 1.0×10^{-3} and 3.6×10^{-3}, respectively and this corresponds to about 0.4% and 1.3% of the 3D turbine power coefficient, respectively. Fig. 6 shows the CFD predictions of both the power coefficients from the turbine mid-span section and the overall turbine power coefficients at a TSR of 2.29. The relative difference between the predicted values based on the baseline mesh and fine meshes is about 1%, which means that further increasing of the mesh size has a very small influence on the numerical result. Therefore, the settings in the baseline mesh are chosen for the further tests.

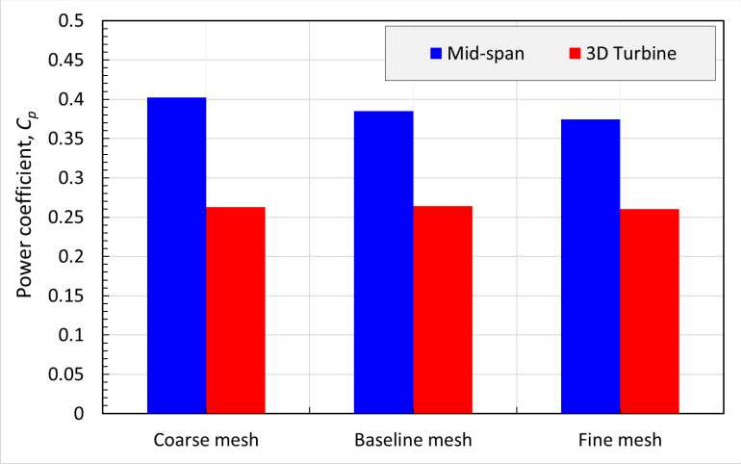

Fig. 6 The prediction of both the power coefficient contribution of the turbine mid-span section and the turbine overall power coefficients for the different meshes at a TSR of 2.29.

2.3.2. 3D VAWT CFD validation using experimental data

The baseline mesh has been chosen to simulate the motion of the VAWT and the results obtained is validated by the experimental data of Li et al. [12]. Both the experiment and the

simulation use the same geometrical and operational characteristics as listed in Table 1 and 2. The experiment in Li et al.'s work [12] is implemented in an open circular type wind tunnel with the six-component balance installed on the basement of wind turbine to measure the force and the moment. The high frequency pressure scanners are located at different positions along the spanwise directions of the rotor blade. Fig. 7 shows a comparison between the CFD predictions of the instantaneous torque coefficient and the corresponding experimental data obtained by the integration of the pressure distribution from the pressure scanner at the blade mid-span [12]. This comparison shows a good agreement between the CFD prediction and the experimental data, which confirms that the numerical setup and the mesh are convincing in the numerical study of the motion of the VAWT. Therefore, the current setup is used to study the effect of the proposed winglet design on the performance and the flow behaviour around the turbine.

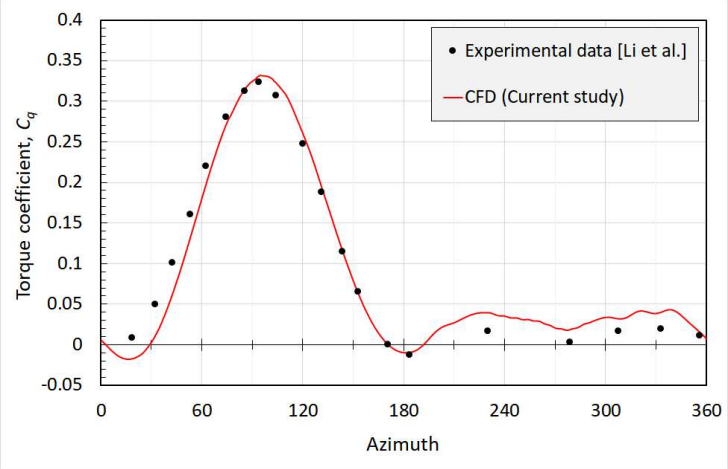

Fig. 7 A comparison between the experimental and the numerical data of the torque coefficient contribution at the turbine mid-span at a TSR of 2.29.

As mentioned in Section 2.2, the winglet design process used the one blade model because this model can save the meshing and simulation cost. Fig. 8 shows the mesh in the flow field and the surface mesh on the blade for the one blade model simulation. This mesh is generated based on the baseline mesh used in the full-scale simulations. The Reynold number, the meshing strategy and the settings in Fluent are all the same with the full-scale simulation.

In this one blade simulation domain, the flow field is divided into 3 parts, namely the outfield, the rotation field around the straight blade and the rotational field around the winglet. It should be noticed that only the third part adopts an unstructured mesh because this can improve the mesh generation efficiency around a morphing winglet. The node number along the profile of the winglet is the same as that on the blade (172 nodes). Since an unstructured mesh is adopted in the subdomain around the winglet, the nodes number is relative with the winglet configuration. The maximum face size in the winglet subdomain is limited to 0.01 meter and the maximum dimensionless wall distance, y+, around the surface is less than 1.2. The grid in the flow field is clustered towards the rotating region in order to capture the flow characteristics more precisely. The encrypted set up is the same with the baseline mesh validated in the full-scale model.

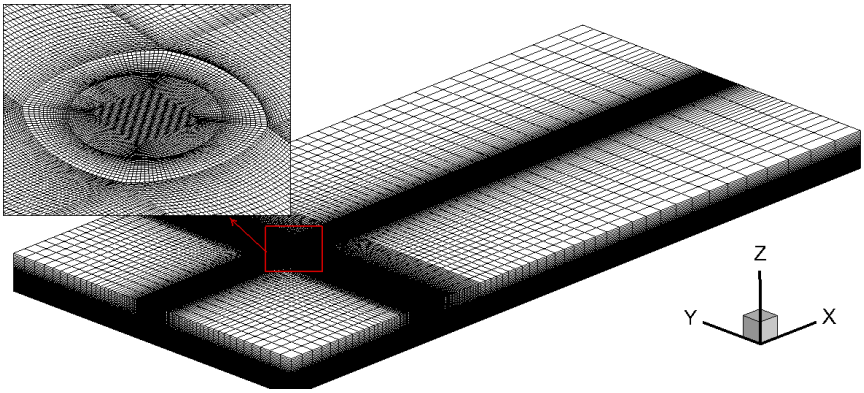

(a) Mesh in the flow field

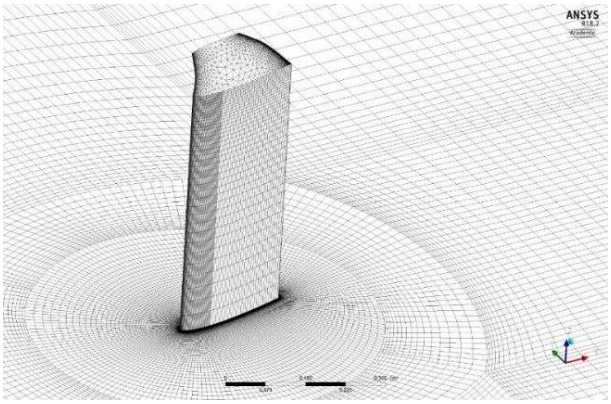

(b) Mesh on the blade and winglet

Fig. 8 Mesh division in the flow field and on the blade.

Since the one blade simulation has to consider the blade's motion and the transient incident velocity, the User-Defined-File (UDF) file and the sliding mesh are adopted based on Ansys Fluent. In the current simulation, the free flow velocity is V_∞=7m/s and the TSR is 2.29 based on Li's experiment [12] so that the rotation speed is ω=18.86/s. The relative incident velocity condition is applied at the velocity inlet, and the incident velocity is defined according to Eq. (9). The rotating part around the blade and the winglet employs a sliding mesh approach and the blade's motion is realized by rotating the mesh around it according to Eq. (5), in which $\theta = \omega \cdot t$. Both the transient incident velocity condition and the rotating mesh are realized by UDF files, which allow users to customize ANSYS FLUENT.

3. Orthogonal experimental design (OED)

3.1. A brief introduction of the OED approach

Orthogonality is an important index in the Design of Experiments (DOE) because it reflects the independence among the design variables. An experimental analysis of an orthogonal design is usually straightforward in that each main effect and the independency of the parameters can be estimated. The OED assists in the sampling among the parameter combinations with multi levels and shows the impact of the parameters when employing only a few experiments. Designers can choose the most influential variables and simplify the optimization process through an orthogonal experiment design. This approach is now commonly used in the energy and aerospace fields, especially in those circumstances when the single experiment or simulation is costly [45-47]. For example, Wang et al. [46] combined the OED method and the CFD approach in optimizing the performance of a three-bladed VAWT with leading-edge serrations and helical blades. Liu et al. [47] applied the OED approach to study the effects of many factors on the optical-thermal efficiency of a parabolic trough solar collector. Since the samples in the OED have orthogonality, they can also be used to establish

a surrogate model before optimization [48-50]. Due to the continual study of OED, different orthogonal arrays that are suitable for different numbers and levels of the variables are now available. This paper adopts the OED method in studying the importance of the design variables and the optimal variable value arrangement in the pre-set level arrays.

There are 6 parameters that define the geometry of the winglet, and these are shown in Fig. 9. This figure shows that there is a dashed line inside of the winglet, and the winglet is generated by sweeping the airfoil along the dashed line. This dashed line composes of an arc and its tangent line. The radius and the radian of the arc, namely R_{cant} and Ω_{cant}, define the radius and radian of the winglet. The length of the tangent line (L_{tip}) defines the length of the winglet, and C_{tip} is the chord length of the airfoil at the tip of the winglet. σ is the twist angle of the winglet after the sweep operation, and its positive direction is noted in the figure. Θ_{sweep} is the sweep angle of the winglet, and it is controlled by the moving of the dashed line along the blade's chord line. In the scope of this paper, the winglet bends towards the inside direction of the rotor of the VAWT. Further, the winglet's airfoil in every section is maintained to be the same as that of the blade's airfoil.

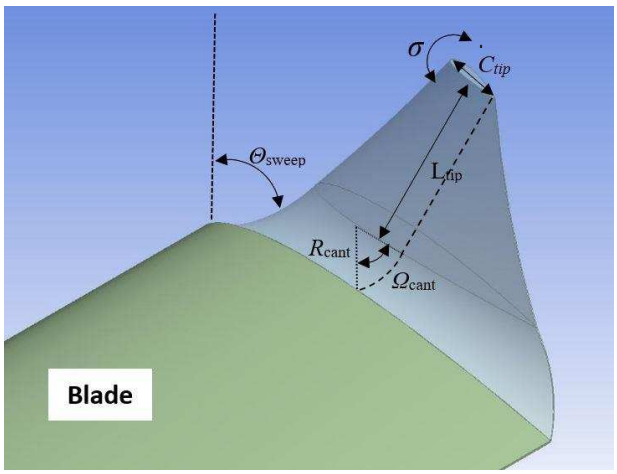

Fig. 9 Schematic diagram of the parameters that define the winglet geometry.

3.2. Design variables, levels and objective of the winglet design

The design variables in the winglet design are mainly based on the design parameters shown in Fig. 9 but with some modifications. For example, Θ_{sweep} is controlled mainly by moving the dashed line along the blade's chord line but also C_{tip} has an impact on Θ_{sweep}. Since C_{tip} is already defined as a design variable, in this paper we use the sweep distance (ϑ_{sweep}) as the design variable. When ϑ_{sweep}= -0.057, the corresponding sweep angle is 0. A larger ϑ_{sweep} value than -0.057 means a positive Θ_{sweep} while a smaller value means a negative Θ_{sweep} (See to Fig. 9). The chord length of the winglet's tip (C_{tip}) is dimensioned by the blade's chord length (C_b), and the ratio of C_{tip} and C_b is defined by γ_{tip}.

Table 4. Design parameters and design levels of the winglet.

Parameters / Levels	L_{tip}(m) Tip length	R_{cant}(m) Cant radius	Ω_{cant}(°) Cant angle	ϑ_{sweep}(m) Sweep distance	γ_{tip} Tip scale	σ(°) Twist angle
Level 1	0.03	0.03	20	-0.09	0.01	-14.4
Level 2	0.04	0.04	40	-0.07	0.15	-7.2
Level 3	0.05	0.05	60	-0.057	0.3	0
Level 4	0.06	0.06	80	0	0.45	7.2
Level 5	0.07	0.07	100	0.03	0.6	14.4

In the OED design of the winglet, the aim is to determine the most significant design variable and the optimal arrangement of the variables. The design variables can be set to be in a wide range but a distorted configuration has a negative impact on the meshing and convergence. As a result, this paper balances the range of the variables and the convergence requirements and divides every parameters into 5 levels. The design variables and the design levels are listed in Table 4. The design levels and ranges of the design variables are chosen to cover as many configurations as possible. However, considering the regularity of the grid and the convergence of the simulations, we have limited these levels to be in an acceptable range.

3.3. $L_{25}(5^6)$ orthogonal array

The combination of the variable values listed in Table 4 results in 5^6=15625 cases to be investigated. However, the Orthogonal Array uses only a few of these combinations to

determine the influence and significance of each variable. In this case, the $L_{25}(5^6)$ orthogonal array is adopted to design the samples, where 'L' stands for the orthogonal array and 25 is the total samples needed in the array [56]. Using 5^6 means that there are 6 design variables in total and each variable has 5 levels. The orthogonal array used in this paper is listed in Table 5. C_p is the power coefficient obtained in each case and C_{p0} is the power coefficient of the blade without a winglet. The value of C_{p0} is 0.0917. The last column in Table 5 reflects the effect of using the winglet in each case.

Table 5. The $L_{25}(5^6)$ standard orthogonal array for the parametric study of the winglet and the power coefficients.

OED No.	L_{tip}(m)	R_{cant}(m)	Ω_{cant}(°)	ϑ_{sweep}(m)	γ_{tip}	σ(°)	C_p(result)	C_p/C_{p0}
1	0.03	0.03	20	-0.09	0.01	-14.4	0.0962	104.9%
2	0.03	0.04	40	-0.07	0.15	-7.2	0.1017	110.9%
3	0.03	0.05	60	-0.057	0.3	0	0.1043	113.7%
4	0.03	0.06	80	0	0.45	7.2	0.0982	107.1%
5	0.03	0.07	100	0.03	0.6	14.4	0.0769	83.9%
6	0.04	0.04	20	-0.057	0.45	14.4	0.0818	89.2%
7	0.04	0.05	40	0	0.6	-14.4	0.1198	130.6%
8	0.04	0.06	60	0.03	0.01	-7.2	0.1141	124.4%
9	0.04	0.07	80	-0.09	0.15	0	0.1103	120.3%
10	0.04	0.03	100	-0.07	0.3	7.2	0.0843	91.9%
11	0.05	0.05	20	0.03	0.15	7.2	0.0987	107.6%
12	0.05	0.06	40	-0.09	0.3	14.4	0.0771	84.08%
13	0.05	0.07	60	-0.07	0.45	-14.4	0.1182	128.9%
14	0.05	0.03	80	-0.057	0.6	-7.2	0.1052	114.7%
15	0.05	0.04	100	0	0.01	0	0.1082	118.0%
16	0.06	0.06	20	-0.07	0.6	0	0.1038	113.2%
17	0.06	0.07	40	-0.057	0.01	7.2	0.0877	95.6%
18	0.06	0.03	60	0	0.15	14.4	0.0832	90.7%
19	0.06	0.04	80	0.03	0.3	-14.4	0.0998	108.8%
20	0.06	0.05	100	-0.09	0.45	-7.2	0.1016	110.8%
21	0.07	0.07	20	0	0.3	-7.2	0.1134	123.7%
22	0.07	0.03	40	0.03	0.45	0	0.1106	120.6%
23	0.07	0.04	60	-0.09	0.6	7.2	0.091	99.2%
24	0.07	0.05	80	-0.07	0.01	14.4	0.0844	92.0%
25	0.07	0.06	100	-0.057	0.15	-14.4	0.1068	116.5%

In order to give an intuitive idea of the winglets' configurations in the array, some examples are shown in Fig. 10. Different configurations have different shadow areas but this effect is considered when presenting the results in the following sections.

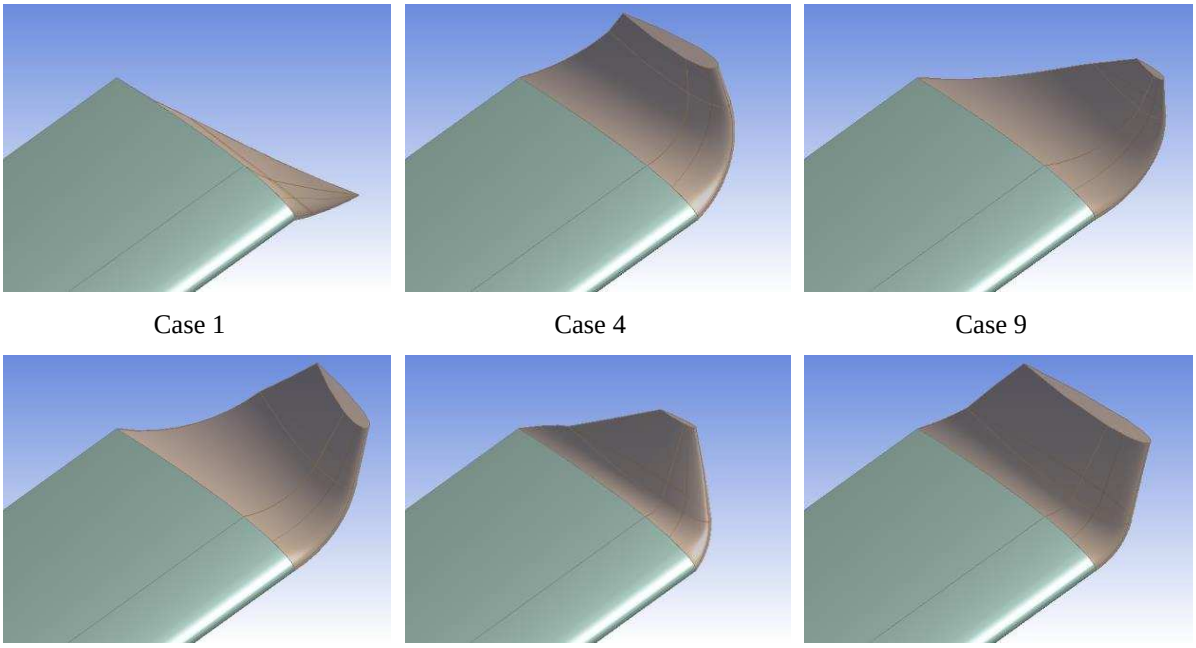

Case 1 Case 4 Case 9

Case 13 Case 18 Case 23

Fig. 10 Some examples of the winglet configurations in the orthogonal array.

4. Results and Discussion

4.1. Analysis of the OED Results

4.1.1. Analysis of the range (ANORA) of the OED results

Table 6. Mean C_p distribution as a function of the different design parameters and different parameter levels.

	L_{tip}	R_{cant}	Ω_{cant}	ϑ_{sweep}	γ_{tip}	σ
L1	0.09546	0.0959	0.09878	0.09524	0.09812	0.10816
L2	0.10206	0.0965	0.09938	0.09848	0.10014	0.1072
L3	0.10148	0.10176	0.10216	0.09716	0.09578	0.10744
L4	0.09522	0.1	0.09958	0.10456	0.10208	0.09198
L5	0.10124	0.1013	0.09556	0.10002	0.09934	0.08068
max	0.10206	0.10176	0.10216	0.10456	0.10208	0.10816
min	0.09522	0.0959	0.09556	0.09524	0.09578	0.08068
average	0.09909	0.09909	0.09909	0.09909	0.09909	0.09909
$R(C_p)$	0.00684	0.00586	0.0066	0.00932	0.0063	0.02748

Since the power coefficients of the 25 cases investigated are listed in Table 5, an analysis of the range is based on these results to assist in the identifying of the significance of the design variables. Table 6 lists the mean power coefficient (Cp) distribution as a function of the different parameters and different levels. $R(C_p)$ is the range between the maximum and minimum values of a specific variable at different levels. It is clear that σ (the twist angle) has the largest $R(C_p)$, which means that the variance of σ has the most significant impact on C_p. The value in the dark shade is the maximum values in each column. These values mean that the power coefficient can be relatively high when the corresponding variables adopt the corresponding levels. Fig. 11 is a graphic display of Table 6, and it reflects the influence of the parameters more clearly.

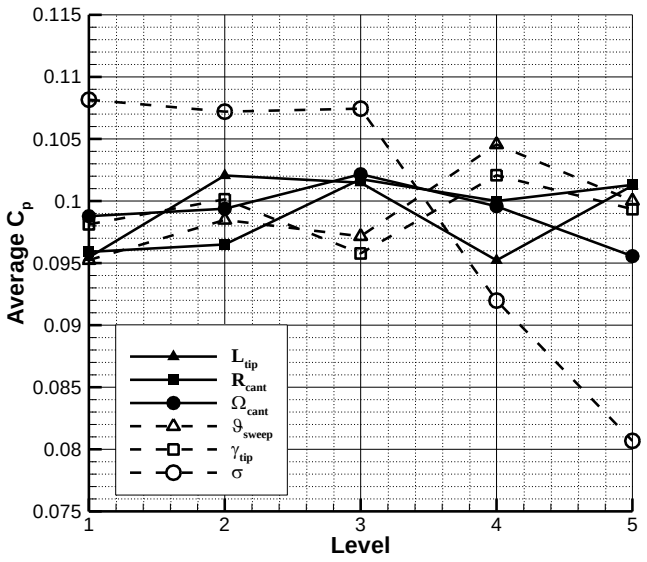

Fig. 11. C_p distribution as a function of the design levels for the 6 design parameters.

Overall, Table 6 and Fig. 11 show the importance in the order of the 6 parameters is $\sigma > \vartheta_{sweep} > L_{tip} > \Omega_{cant} > \gamma_{tip} > R_{cant}$ and their optimal levels are L1, L4, L2, L3, L4, L3, respectively. The corresponding optimal value for the design variables in the current range are as follows:

$$\sigma=-14.4^{\circ},\quad \vartheta_{sweep}=0\text{m},\quad L_{tip}=0.04\text{m},\quad \Omega_{cant}=60^{\circ},\quad \gamma_{tip}=0.45,\quad R_{cant}=0.05\text{m}$$

4.1.2. Analysis of the variance (ANOVA) of the OED results

The ANOVA is used to estimate the relative significance of each parameter in terms of the percentage contribution to the overall response. It reflects the design parameters that have a significant impact on the results.

Table 7 lists the ANOVA results and the parameters in the analysis process. The sum of the squares of the deviations that are specific to one variable is divided into the sum of the squares within the group (SSW) and the sum of the squares between the groups (SSB) [57, 58]. The degree of freedom within each group (DoFW) is the value of that observation number minus the group number. The degree of freedom between the groups (DoFB) is the value of that group number minus 1. F_{value} is determined as follows:

$$F_{value} = \frac{SSB/DoFB}{SSW/DoFW} \tag{11}$$

Table 7. The data employed in the analysis steps in the study of the parameter significance.

	L_{tip}	R_{cant}	Ω_{cant}	ϑ_{sweep}	γ_{tip}	σ
SSW	0.003655	0.003743	0.003780	0.003643	0.003781	0.000855
SSB	0.000237	0.000149	0.000112	0.000249	0.000110	0.003036
DoFW	20	20	20	20	20	20
DoFB	4	4	4	4	4	4
F_{value}	0.3236	0.1985	0.1475	0.3411	0.1455	17.7505
$F_{0.05}$	2.8661	2.8661	2.8661	2.8661	2.8661	2.8661
significance	0	0	0	0	0	1

The standard F value is determined from an F-table for a given statistical level of the significance. In this paper, the standard F value at the 5% significance level is 2.8661 when the DoFW and DoFB are 20 and 4, respectively [59]. When the F_{value} of a specific variable is greater than the standard value $F_{0.05}$, then this means that this variable is significant. In Table 7, the F_{value} of the twist angle (σ) is 17.75056, which is larger than $F_{0.05}$. The F_{value}s for the other variables are all smaller than $F_{0.05.}$ Therefore, the ANOVA result reflects that σ is the only

significant factor among all the chosen design variables. This result is consistent with the ANORA result. This means that when the optimization of the winglet's configuration is required in the following work, the twist angle should be the most important parameter to consider.

4.2. Working mechanism analysis of the winglet

As discussed in Section 4.1.1, the best arrangement for the design variables in the current range are as follows:

$$\sigma=-14.4^{\circ},\quad \vartheta_{sweep}=0\text{m},\quad L_{tip}=0.04\text{m},\quad \Omega_{cant}=60^{\circ},\quad \gamma_{tip}=0.45,\quad R_{cant}=0.05\text{m}$$

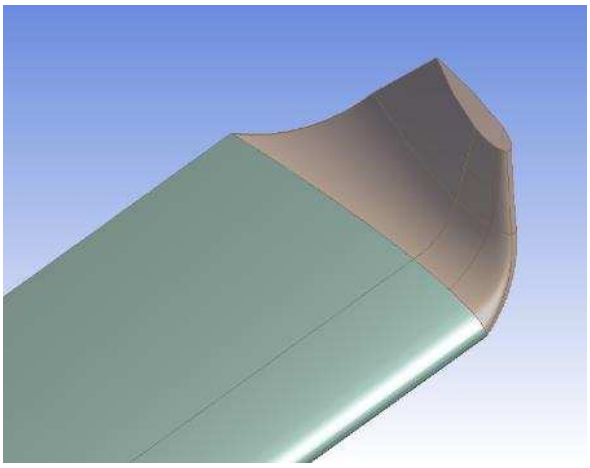

Fig. 12 The designed winglet using the optimal variable level arrangement.

Fig. 12 shows the winglet configuration in the optimal data set. The aerodynamic performance for this configuration is calculated and compared with the non-winglet blade (reference blade) in the following sections.

4.2.1. Comparison of the best result and the reference blade

Fig. 13 shows a comparison of the tangential and normal force coefficients as a function of the azimuthal angle between the reference blade and the blade with the optimized winglet. The corresponding angle of attack can be calculated using Eq. (5). The figure shows that both the tangential and normal force coefficients of the blade with the optimal winglet have higher

maximum values than the reference value. Further, their values are almost the same when the azimuthal angle is 0°and 180° but the difference becomes larger when the azimuthal angle approaches 90° and 270°. The same characteristics appear in the torque coefficient comparison in Fig. 14.

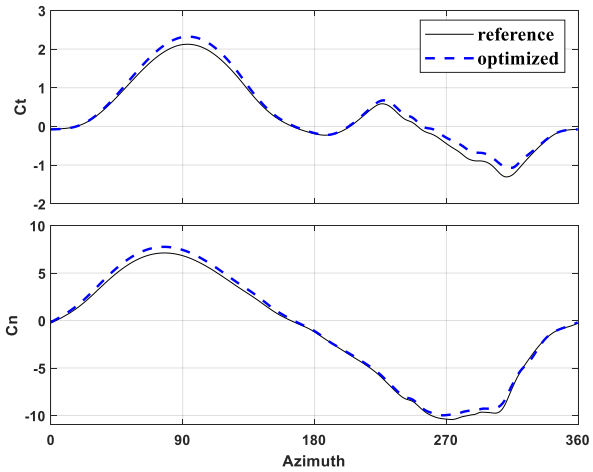

Fig. 13 Comparison of the tangential and normal force coefficients as a function of the azimuthal angle between the reference blade and the blade with the optimized winglet.

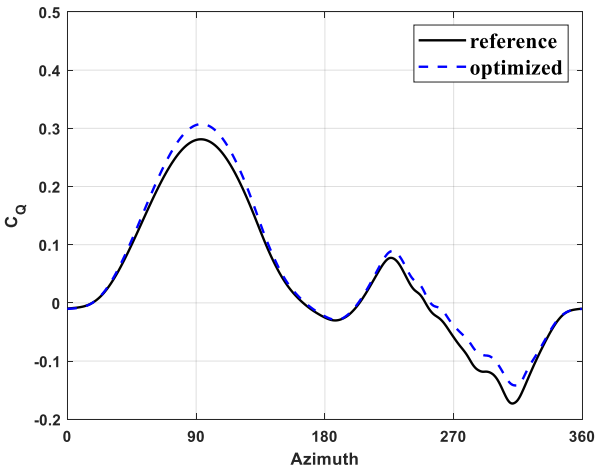

Fig. 14 Comparison of the torque coefficients as a function of the azimuthal angle between the reference blade and the blade with the optimized winglet.

The results above can be explained by Fig. 15 and Fig. 16, in which the flow field characteristics are compared separately when the azimuthal angle is 90° and 180°, respectively. In Fig. 15, the near-tip streamlines derived from the upstream of the reference blade transfer from the pressure side to the suction side at the blade tip. This phenomenon results in the pressure difference between the two sides of the blade becoming smaller and the blade cannot effectively use the pressure difference to generate thrust. The winglet separates both sides of the blade so that most of the streamlines cannot cross the blade tip, which maintains the pressure difference between the two sides of the blade and this improves the aerodynamic efficiency of the surface near the blade tip. In Fig. 16, the near-tip streamlines of the reference blade do not cross the blade tip so that the winglet's function is not obvious. The reason is that the attack angle of the blade is small when the azimuthal angle is 180° and the pressure difference of both sides is not apparent. As a result, the winglet improves the blade's

aerodynamic performance when the azimuthal angle is 90° but the improvement is not obvious when the azimuthal angle is 180°. The reason why the winglet improves the blade's performance at the azimuthal angle around 300° is similar to that when the azimuthal angle is 90°. Since the one-blade model does not consider the wake of the rotor, the flow contours when the azimuthal angle ranges from 180° to 360° is not discussed in this section. Following section, where full rotor model simulations have been implemented, will further compare the results.

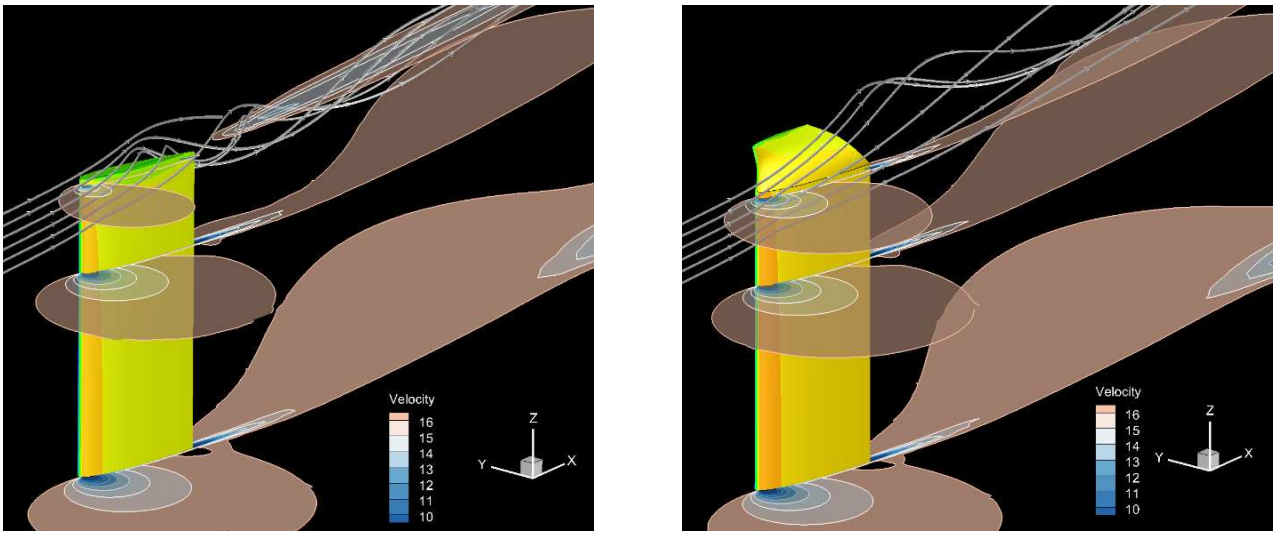

Fig. 15 The flow field characteristics when the azimuthal angle is 90°.
(Left side: the reference blade, right side: the blade with the optimal winglet)

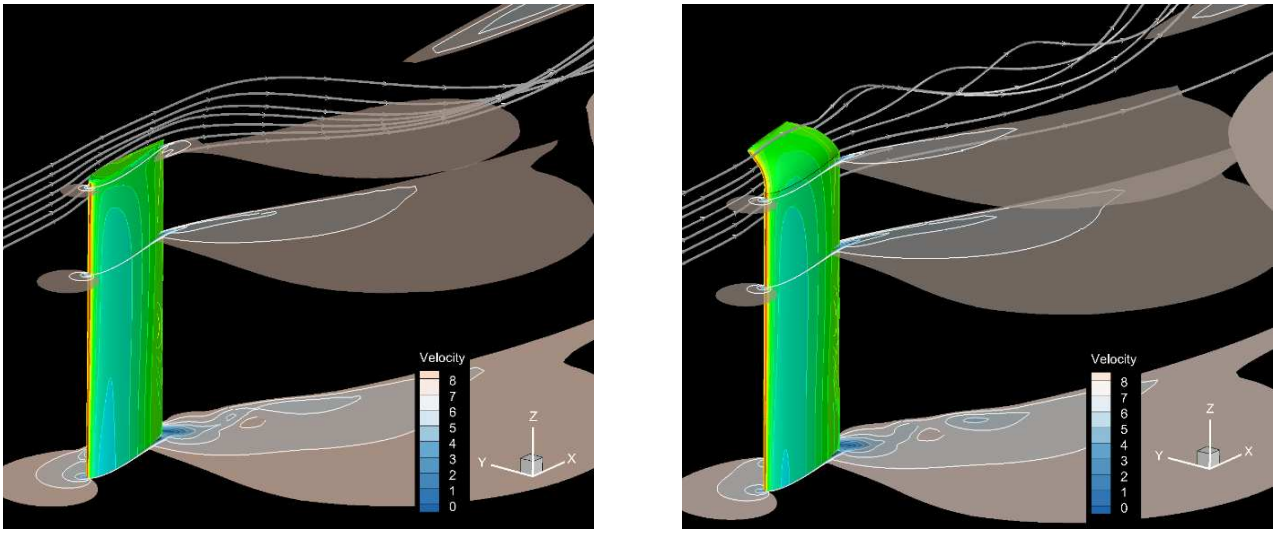

Fig. 16 The flow field characteristics when the azimuthal angle is 180°.
(Left side: the reference blade, right side: the blade with the optimal winglet)

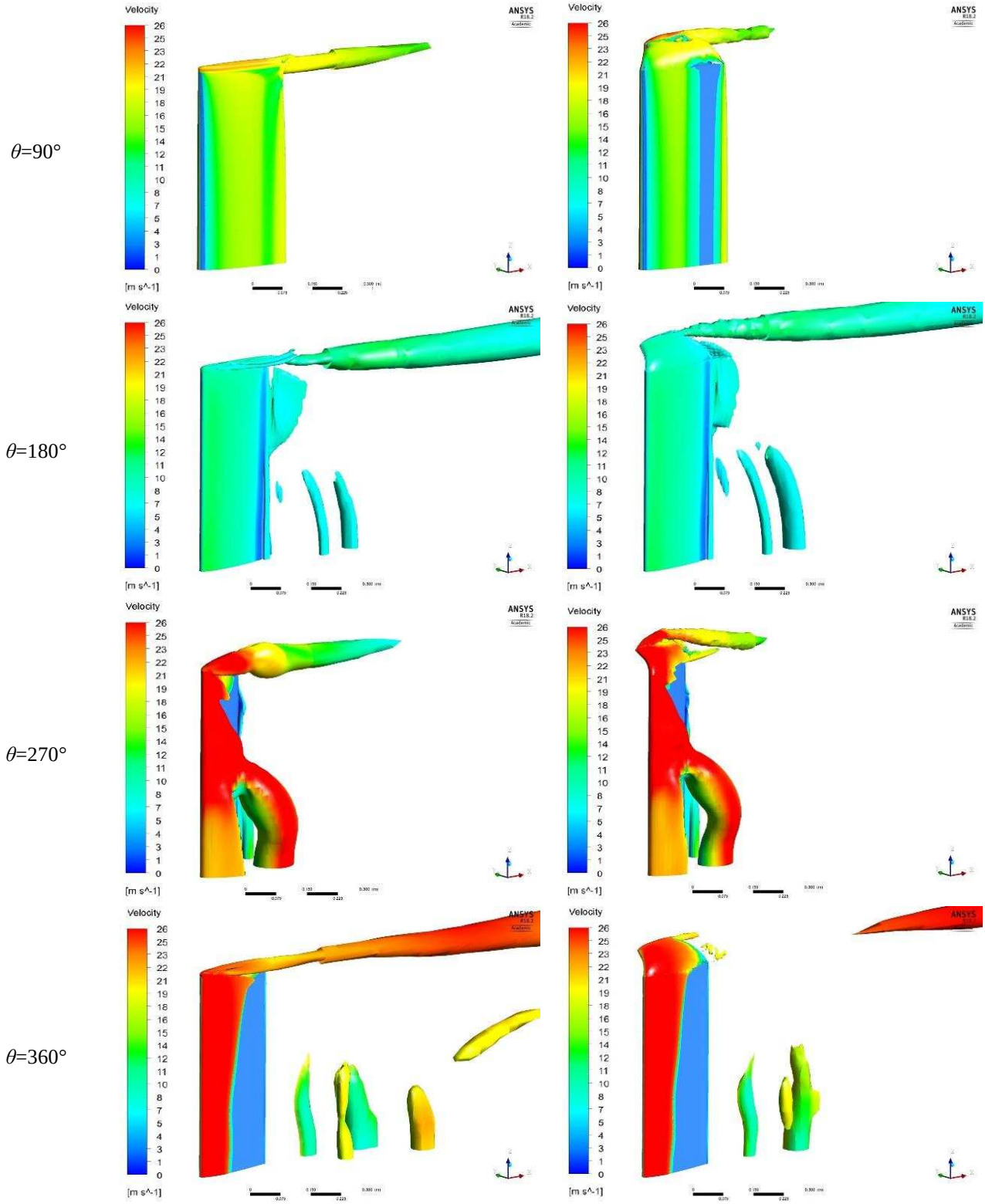

Fig. 17 Iso-surface contours for the Q-criterion (Q level= 0.005) coloured by the norm of the resultant velocity. (The left column is the result for the reference blade; the right column is the result for the blade with the optimal winglet.)

Fig. 14 also shows that the torque coefficient of the optimized configuration has a higher maximum value and average value than the reference blade. As a result, the power

coefficient for the designed blade is larger than the reference value. In the current study, the power coefficient of the optimized configuration is 0.1207, which is 31.6% higher than the power coefficient of the reference blade (0.0917). This means that the winglet can greatly improve the power efficiency of the VAWT's blade.

Fig. 17 shows a comparison of the iso-surface contours between the optimized configuration and the reference blade when the Q-criterion level is 0.005. The Q-criterion is a method to describe the instantaneous vortex structures, which reflects the 3D structures of the flow field [60]. The iso-surface is coloured by the norm of the resultant velocity of the flowfield. In the same flow condition, a longer vortex structure means a stronger vortex strength and a more revere pressure interaction at the blade tip. Since the pressure interaction at the blade tip reduces the pressure difference between two sides of the blade, and thus decrease the power efficiency, a reduced vortex length can visually reflect a weaker pressure interaction phenomenon and an improvement in the power efficiency. The first column is the result for the reference blade and the second column is the result for the blade with the optimal winglet. Fig. 17 shows that when the azimuthal angle is 90°, the optimized configuration's vortex area is smaller than the reference blade's vortex area. Also the same phenomenon appears when the azimuthal angle is 270° and 360°. The contours for both configurations are similar when the azimuthal angle is 180°. Fig. 18 compares the contours of the vorticities in the normal and lateral planes when the azimuthal angle is 90°. The contours are sliced in the same position for both the reference blade flow filed and the blade with winglet flow field. These figures show that the winglet can change the distribution of the vorticity field and decrease the intensity and the influence area of the tip vortex. The results presented in both Fig. 17 and Fig. 18 show that the tip vortex of the blade can be weakened by appending the optimized winglet on the blade during most part of the rotation cycle. This means that a drop in the pressure interaction

appears at the end of the blade when the winglet is adopted. Therefore, the power efficiency of the blade is improved.

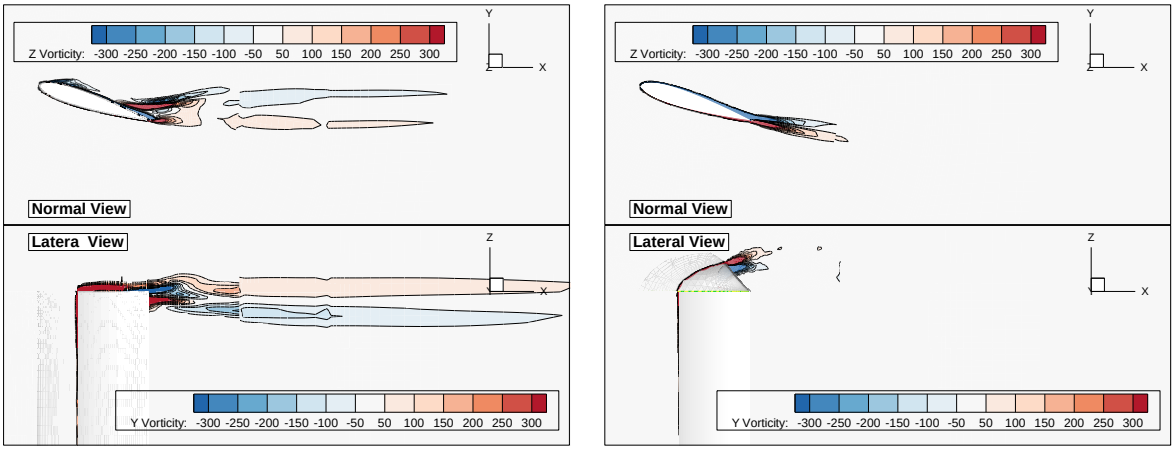

(a) The reference blade (b) The blade with the designed winglet

Fig. 18 The contours of the turbulence kinetic energy in normal and lateral planes when $\theta = 90°$

4.2.2. Full rotor model simulation of the winglet in the OED result

The winglet design process and the result comparison above are all based on the one blade simulation model. We have mentioned in Section 2.1 that the one-blade model is a simplification of the full-scale VAWT model, and it does not consider the wake of the rotor. In order to validate the practical influence of the proposed winglet on the performance of the turbine, the full-rotor VAWT model with the proposed winglet amended to the turbine is simulated in this section. The computational domain and the full-rotor mesh have been shown in Fig. 4 and Fig. 5 and the accuracy of this full-rotor VAWT model has been validated as shown in Fig. 7. It is found that amended winglet increases the height of the blade by about 14.6% and therefore this changes the swept area of the rotor. In calculating the aerodynamic coefficients of the turbine, the modified swept area of the model is shown in Fig. 19 and is bounded by the blade profile trace line. Fig. 20 and Fig. 21 are the numerical results based on the full-rotor model and the simulations by considering the blade-blade interaction and blade-shaft interaction, thus making it more in line with the actual situation.

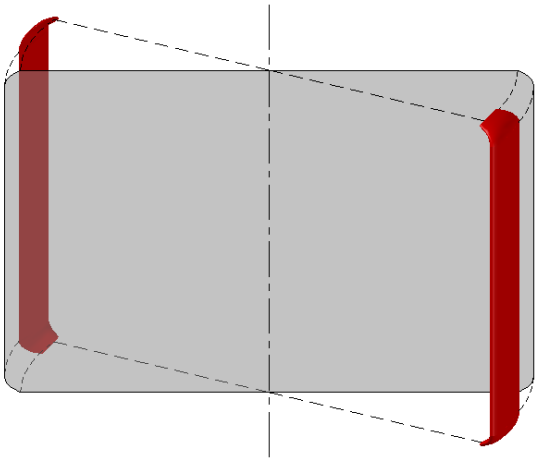

Fig. 19 An illustration of the swept area of the turbine with the selected winglet.

Fig. 20 shows the torque coefficients with and without the proposed winglet at different spanwise locations for a TSR of 2.29. The lines with symbols on them are the results acquired by the full rotor simulation with winglets on the blades while the other lines are the results acquired by the full rotor simulation without the winglets. Different line types stand for the results acquired on different spanwise sections. It should be noted that the presence of the winglet at the blade tip enhances the torque contribution along the blade span. The specific improvement of power coefficients at the mid-span profile, the profiles at $z=0.7 \cdot H/2$ and $z=0.8 \cdot H/2$ are 1.3%, 9.8% and 16%, respectively. More enhancement is achieved near the blade tip because the pressure transection in the blade tip has more severe impact on the blade surface close to the tip. The winglet separates the pressure side and the suction side of the blade in the tip, and the tip vortex is weakened. Therefore, the pressure distribution difference on the blade along the span wise direction is decreased and the closer to the blade's tip, the more obvious the improvement appears. In addition, Fig. 20 also shows that the performance improvement appears mainly at the upstream stage (when the azimuthal angle ranges from 0° to 180°) of the rotor and the difference among the torque coefficients at the downstream stage is not obvious.

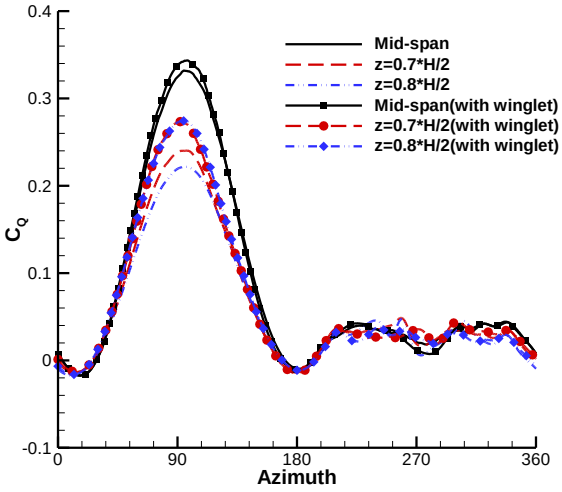

Fig. 20 A comparison between the torque coefficient contribution for different spanwise locations at a TSR of 2.29 with and without the proposed winglet.

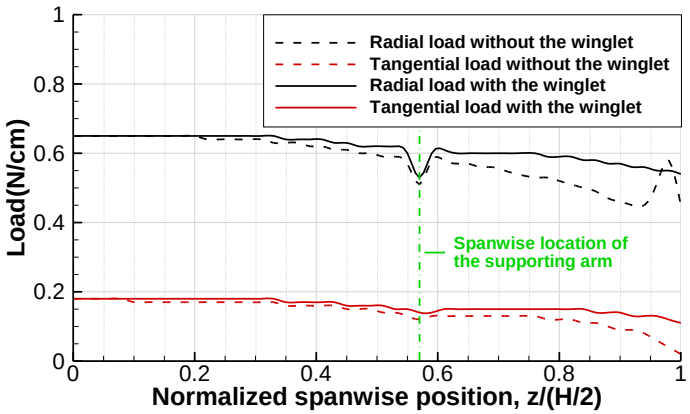

Fig. 21 Specific blade loading on blades with and without a winglet at an azimuthal angle of 90°.

Fig. 21 shows the blade loading at an azimuthal angle of 90°, which approximately corresponds to the azimuthal location of the maximum instantaneous power coefficient. A drop of radial load appears at the span wise location of the supporting arm. The near tip jump of the radial load for the blade without a winglet is caused by the secondary flow effect, namely "Blade tip leakage flow", and it is eliminated by the winglet. It appears that the overall blade loading did not significantly change but the radial and tangential blade values are more evenly distributed along the span wise direction with the influence of the winglet. The average increase in the radial and tangential blade loading with a winglet are about 6% and 15%, respectively.

Fig. 22 shows the enhancement of the overall power coefficient due to the use of the winglet for three different TSRs. The relative power coefficient enhancements of the blade with a winglet are about 10.5%, 6.7% and 10.0% for TSRs of 1.85, 2.29 and 2.52, respectively. This means that although the winglet is designed under the condition that the TSR is 2.29, it can improve the VAWT's power coefficient under other TSR conditions. As a result, adding the designed winglet on the blade tip is a good choice to enhance the overall performance of the VAWT.

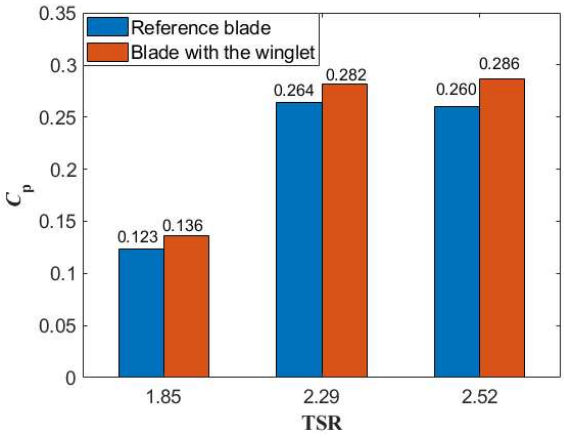

Fig. 22 The influence of the winglet on the turbine power coefficient at different TSRs.

4.3. Discussion of the results

In this paper, we have used six parameters for the design variables in defining the winglet's configuration. Although this paper is not designed to optimize the winglet configuration, the adopted OED approach discovered the most influential design parameter and obtained a winglet with a recommended parameter arrangement. Since the winglet is a 3D configuration, it requires many parameters in the design process. The results in the OED analysis show that the twist angle is the most influential parameter so that special attention should be paid on the twist angle in the primary optimization of the winglet configuration.

The designed winglet has been proved to be beneficial for both the one blade model and the full-scale VAWT rotor. According to the full-scale rotor simulation results, the winglet enhances the rotor's power coefficient by 10.5%, 6.7% and 10.0% for TSRs of 1.85, 2.29 and 2.52, respectively. Although the design process is implemented in the condition that the TSR is 2.29, the obtained winglet improves the power coefficients at other TSR conditions. This means that the turbine's efficiency is enhanced in different free flow conditions by installing the winglet on the tip. The development of the tip vortex can directly reflect the pressure interaction at the blade tip. Through a flow contour comparison, we find that the winglet enhances the turbine's power efficiency by separating the pressure side and the suction side of the blade and maintaining the pressure difference on the blade. The power performance comparison at different locations along the span wise direction of the blade reflects that the performance enhancement is increasingly obvious as it approaches the blade tip.

On adding the designed winglet in this work onto the blade tip will increase the blade volume by 11.7% and of course this will increase the cost of the blade. The real cost increment will depend on the manufacturing technique employed. For example, the 3D print technique can be used to produce winglets for small-scale turbines, and for large-scale turbines, the manufacturing of the winglet can refer to the turbine blade manufacturing technique. These technologies are very mature now and will not increase the cost too much. When considering all the other parts of a VAWT system then the percentage increase in the cost will be very small. In addition, the winglet can be designed and manufactured separately from the blade and be appended on the blade tip during installation. This makes it easy to produce, maintain and replace. Further, winglets have already been very successfully used on the tip of aircraft wings and the blades of some HAWTs. This means that there are available techniques to consult in manufacturing and installing the winglet onto the blade tip of the VAWT. Since the blade of

the VAWT is even simpler than the aircraft wing and the working environment is less harsh than that of the aircraft, it is feasible to use a winglet.

5. Conclusion

This paper numerically studies the configuration of the winglet on the power performance of VAWTs. Based on the OED approach, the significance of the design variables have been investigated, and the optimal variable level arrangement is obtained in order to generate an optimal configuration to compare with the non-winglet blade. From the results presented in this paper, we draw the following conclusions:

(1) The twist angle is the most significant design parameter in the current parametric approach with an F value of 17.75 while the F_{value}s for the other design variables are all smaller than $F_{0.05}$. It is seen that the power performance of the winglet increases with the absolute value of negative twist angle.

(2) The winglet with the optimal design variable arrangement can decrease the magnitude of the tip vortex of the blade by maintaining the pressure difference between two sides of the blade and thus improve the power coefficient. The power output of the VAWT, as well as the power improvement by the winglet, mainly occurs in the upstream stage because the blade-blade interaction and the blade-shaft interaction of the VAWT make the downstream performance incomparable with the upstream stage.

(3) The improvement in the aerodynamic performance of VAWTs by the winglet becomes increasingly more obvious when it gets closer to the blade tip along the span wise direction. The specific improvement of the power coefficient increases from 1.3% to 16% from the mid-span profile to the profile at $z=0.8 \cdot H/2$. This is because the pressure interaction at the

blade tip region has an influence mainly on the near tip region and adding the winglet onto the blade tip can reduce the pressure interaction.

(4) An improvement in efficiency of about 6.7% could be achieved by the designed winglet at the optimal TSR while up to 10% of improvement could be achieved in off-design TSRs. Thus adding the winglet onto the blade's tip is beneficial for enhancing the efficiency of the VAWT in different wind conditions.

Acknowledgement

Tiantian Zhang would like to acknowledge the China Scholarship Council and the University of Sheffield for funding his research studies. Mohamed M. Elsakka would like to express his gratitude to the Egyptian Cultural Affairs and Missions Sector along with Port Said University for their financial support. The authors also acknowledge the support from the National Natural Science Foundation of China (Nos.11802340 and 11502291).

References

[1] H. Meng, M. Wang, O. Olumayegun, X. Luo, X. Liu. Process design, operation and economic evaluation of compressed air energy storage (CAES) for wind power through modelling and simulation. Renewable Energy. 136 (2019) 923-36.

[2] M. Ghasemian, Z.N. Ashrafi, A. Sedaghat. A review on computational fluid dynamic simulation techniques for Darrieus vertical axis wind turbines. Energy Conversion and Management. 149 (2017) 87-100.

[3] D. MacPhee, A. Beyene. Recent advances in rotor design of vertical axis wind turbines. Wind Engineering. 36 (2012) 647-66.

[4] M.M. Aslam Bhutta, N. Hayat, A.U. Farooq, Z. Ali, S.R. Jamil, Z. Hussain. Vertical axis wind turbine – A review of various configurations and design techniques. Renewable and Sustainable Energy Reviews. 16 (2012) 1926-39.

[5] T. Maître, E. Amet, C. Pellone. Modeling of the flow in a Darrieus water turbine: Wall grid refinement analysis and comparison with experiments. Renewable Energy. 51 (2013) 497-512.

[6] A. Tummala, R.K. Velamati, D.K. Sinha, V. Indraja, V.H. Krishna. A review on small scale wind turbines. Renewable and Sustainable Energy Reviews. 56 (2016) 1351-71.

[7] Q. Li, T. Maeda, Y. Kamada, J. Murata, K. Furukawa, M. Yamamoto. Effect of number of blades on aerodynamic forces on a straight-bladed Vertical Axis Wind Turbine. Energy. 90 (2015) 784-95.

[8] Q. Li, T. Maeda, Y. Kamada, J. Murata, K. Shimizu, T. Ogasawara, et al. Effect of solidity on aerodynamic forces around straight-bladed vertical axis wind turbine by wind tunnel experiments (depending on number of blades). Renewable Energy. 96 (2016) 928-39.

[9] Q. Li, T. Maeda, Y. Kamada, J. Murata, M. Yamamoto, T. Ogasawara, et al. Study on power performance for straight-bladed vertical axis wind turbine by field and wind tunnel test. Renewable Energy. 90 (2016) 291-300.

[10] Q. Li, T. Maeda, Y. Kamada, T. Ogasawara, A. Nakai, T. Kasuya. Investigation of power performance and wake on a straight-bladed vertical axis wind turbine with field experiments. Energy. 141 (2017) 1113-23.

[11] Y. Yang, Z. Guo, Q. Song, Y. Zhang, Q. Li. Effect of blade pitch angle on the aerodynamic characteristics of a straight-bladed vertical axis wind turbine based on experiments and simulations. Energies. 11 (2018).

[12] Q.a. Li, T. Maeda, Y. Kamada, J. Murata, T. Kawabata, K. Shimizu, et al. Wind tunnel and numerical study of a straight-bladed vertical axis wind turbine in three-dimensional analysis (Part I: For predicting aerodynamic loads and performance). Energy. 106 (2016) 443-52.

[13] R. Lanzafame, S. Mauro, M. Messina. 2D CFD Modeling of H-Darrieus Wind Turbines Using a Transition Turbulence Model. Energy Procedia. 45 (2014) 131-40.

[14] A. Rezaeiha, H. Montazeri, B. Blocken. Characterization of aerodynamic performance of vertical axis wind turbines: Impact of operational parameters. Energy Conversion and Management. 169 (2018) 45-77.

[15] A. Rezaeiha, H. Montazeri, B. Blocken. Towards accurate CFD simulations of vertical axis wind turbines at different tip speed ratios and solidities: Guidelines for azimuthal increment, domain size and convergence. Energy Conversion and Management. 156 (2018) 301-16.

[16] A. Rezaeiha, I. Kalkman, B. Blocken. Effect of pitch angle on power performance and aerodynamics of a vertical axis wind turbine. Applied Energy. 197 (2017) 132-50.

[17] C. Li, Y. Xiao, Y.L. Xu, Y.X. Peng, G. Hu, S. Zhu. Optimization of blade pitch in H-rotor vertical axis wind turbines through computational fluid dynamics simulations. Applied Energy. 212 (2018) 1107-25.

[18] D.L. Shukla, A.U. Mehta, K.V. Modi. Dynamic overset 2D CFD numerical simulation of a small vertical axis wind turbine. International Journal of Ambient Energy. (2018).

[19] M. Jafaryar, R. Kamrani, M. Gorji-Bandpy, M. Hatami, D.D. Ganji. Numerical optimization of the asymmetric blades mounted on a vertical axis cross-flow wind turbine. International Communications in Heat and Mass Transfer. 70 (2016) 93-104.

[20] J. Thé, H. Yu. A critical review on the simulations of wind turbine aerodynamics focusing on hybrid RANS-LES methods. Energy. 138 (2017) 257-89.

[21] S.H. Hezaveh, E. Bou-Zeid, M.W. Lohry, L. Martinelli. Simulation and wake analysis of a single vertical axis wind turbine. Wind Energy. 20 (2017) 713-30.

[22] K.H. Wong, W.T. Chong, S.C. Poh, Y.C. Shiah, N.L. Sukiman, C.T. Wang. 3D CFD simulation and parametric study of a flat plate deflector for vertical axis wind turbine. Renewable Energy. 129 (2018) 32-55.

[23] K.H. Wong, W.T. Chong, N.L. Sukiman, Y.C. Shiah, S.C. Poh, K. Sopian, et al. Experimental and simulation investigation into the effects of a flat plate deflector on vertical axis wind turbine. Energy Conversion and Management. 160 (2018) 109-25.

[24] I. Hashem, M.H. Mohamed. Aerodynamic performance enhancements of H-rotor Darrieus wind turbine. Energy. 142 (2018) 531-45.

[25] M.S. Siddiqui, N. Durrani, I. Akhtar. Quantification of the effects of geometric approximations on the performance of a vertical axis wind turbine. Renewable Energy. 74 (2015) 661-70.

[26] A. Abdulrahim, E. Anik, O. Uzol. Effects of Mie Vanes and Tip Injection on the Performance and Wake Characteristics of a HAWT. 34th Wind Energy Symposium2016. p. 0519.

[27] Z. Dong. Effects of Tip Vanes on Aerodynamic Performance of H-Type VAWT. IOP Conference Series: Earth and Environmental Science. IOP Publishing2018. p. 042138.

[28] M. Islam, A. Fartaj, R. Carriveau. Analysis of the Design Parameters Related to a Fixed-Pitch Straight-Bladed Vertical Axis Wind Turbine. Wind Engineering. 32 (2008) 491-507.

[29] Y. Shimizu, H. Imamura, S. Matsumura, T. Maeda, G. Van Bussel. Power augmentation of a horizontal axis wind turbine using a Mie type tip vane: velocity distribution around the tip of a HAWT blade with and without a Mie type tip vane. Journal of solar energy engineering. 117 (1995) 297-303.

[30] Y. Shimizu, E. Ismaili, Y. Kamada, T. Maeda. Power augmentation of a HAWT by Mie-type tip vanes, considering wind tunnel flow visualisation, blade-aspect ratios and Reynolds number. Wind Engineering. 27 (2003) 183-94.

[31] L. Shoutu, W. Yin, Y. Congxin, L. Ye. Numerical Investigation the Effect of the Different Tip Vanes on the Loading of an H-VAWT. E3S Web of Conferences. EDP Sciences2018. p. 03041.

[32] C. Rohmann-Shaw. The Effects of Blade Tip Design on the Aerodynamic Performance of the Vertical-Axis Wind Turbine Blade. Mechnical Engineering. The University of Sheffield, Sheffield, 2016.

[33] E.S. Abdelghany, E.E. Khalil, O. Abdelatif, G. Elharriry. Aircraft Winglet Design and performance: Cant angle effect. Journal of Robotics and Mechanical Engineering Research. 1 (2016) 28-34.

[34] S. Pooladsanj, M. Tadifar. Numerical Study of Winglet at Low Reynolds Numbers. Proceedings of the ASME 2013 Fluids Engineering Summer Meeting, Nevada, USA, 2013.

[35] A. Elham, M.J.L. van Tooren. Winglet multi-objective shape optimization. Aerospace Science and Technology. 37 (2014) 93-109.

[36] A.T. Krebs, B.D.G. Bramesfeld. Using an optimisation process for sailplane winglet design. The Aeronautical Journal. 120 (2016) 1726-45.

[37] R. Yadav, S. Kumar, S. Lakshminarayana, I. Rathlamwala, B. Rathlamwala. Computational Analysis for Random Winglet Designs on Light Aircraft. Journal of Advanced Research in Mechanical Engineering and Technology. 5 (2018) 1-16.

[38] G. Narayan, B. John. Effect of winglets induced tip vortex structure on the performance of subsonic wings. Aerospace Science and Technology. 58 (2016) 328-40.

[39] A. Gupta, R.S. Amano. CFD Analysis of Wind Turbine Blade With Winglets. Proceedings of the ASME 2012 International Design Engineering Technical Conferences & Computers and Information in Engineering Conference, Chicago, IL, USA, 2012.

[40] J. Johansen, N.N. Sørensen. Aerodynamic investigation of Winglets on Wind Turbine Blades using CFD. Risø National Laboratory, Roskilde, Denmark, 2006.

[41] A. Farhan, A. Hassanpour, A. Burns, Y.G. Motlagh. Numerical study of effect of winglet planform and airfoil on a horizontal axis wind turbine performance. Renewable Energy. 131 (2019) 1255-73.

[42] S. Shamsoddin, F. Porté-Agel. A Large-Eddy Simulation Study of Vertical Axis Wind Turbine Wakes in the Atmospheric Boundary Layer. Energies. 9 (2016).

[43] J. Tao, G. Sun, J. Si, Z. Wang. A robust design for a winglet based on NURBS-FFD method and PSO algorithm. Aerospace Science and Technology. 70 (2017) 568-77.

[44] T.-t. Zhang, Z.-g. Wang, W. Huang, L. Yan. A review of parametric approaches specific to aerodynamic design process. Acta Astronautica. 145 (2018) 319-31.

[45] J. Tang, G. Gong, H. Su, F. Wu, C. Herman. Performance evaluation of a novel method of frost prevention and retardation for air source heat pumps using the orthogonal experiment design method. Applied Energy. 169 (2016) 696-708.

[46] Z. Wang, Y. Wang, M. Zhuang. Improvement of the aerodynamic performance of vertical axis wind turbines with leading-edge serrations and helical blades using CFD and Taguchi method. Energy Conversion and Management. 177 (2018) 107-21.

[47] X. Liu, J. Huang, Q. Mao. Sensitive analysis for the efficiency of a parabolic trough solar collector based on orthogonal experiment. International Journal of Photoenergy. 2015 (2015).

[48] L. Yan, W. Huang, T.-t. Zhang, H. Li, X.-t. Yan. Numerical investigation of the nonreacting and reacting flow fields in a transverse gaseous injection channel with different species. Acta Astronautica. 105 (2014) 17-23.

[49] M. Ou, L. Yan, W. Huang, T.-t. Zhang. Design exploration of combinational spike and opposing jet concept in hypersonic flows based on CFD calculation and surrogate model. Acta Astronautica. 155 (2019) 287–301.

[50] W. Huang, J. Yang, L. Yan. Multi-objective design optimization of the transverse gaseous jet in supersonic flows. Acta Astronautica. 93 (2014) 13-22.

[51] N. Ma, H. Lei, Z. Han, D. Zhou, Y. Bao, K. Zhang, et al. Airfoil optimization to improve power performance of a high-solidity vertical axis wind turbine at a moderate tip speed ratio. Energy. 150 (2018) 236-52.

[52] M.M. Elsakka, D.B. Ingham, L. Ma, M. Pourkashanian. CFD analysis of the angle of attack for a vertical axis wind turbine blade. Energy Conversion and Management. 182 (2019) 154-65.

[53] A. Bianchini, F. Balduzzi, G. Ferrara, L. Ferrari. Virtual incidence effect on rotating airfoils in Darrieus wind turbines. Energy Conversion and Management. 111 (2016) 329-38.

[54] Fluent. ANSYS. 18.2 User's Guide, Ansys Inc., 2017.

[55] P.J. Roache. Quantification of uncertainty in computational fluid dynamics. Annual review of fluid Mechanics. 29 (1997) 123-60.

[56] W. Huang, M. Pourkashanian, L. Ma, D.B. Ingham, S.-b. Luo, Z.-g. Wang. Effect of geometric parameters on the drag of the cavity flameholder based on the variance analysis method. Aerospace Science and Technology. 21 (2012) 24-30.

[57] W. Huang, Z.-g. Wang, D.B. Ingham, L. Ma, M. Pourkashanian. Design exploration for a single expansion ramp nozzle (SERN) using data mining. Acta Astronautica. 83 (2013) 10-7.

[58] W. Huang. Design exploration of three-dimensional transverse jet in a supersonic crossflow based on data mining and multi-objective design optimization approaches. International Journal of Hydrogen Energy. 39 (2014) 3914-25.

[59] R.K. Roy. A primer on the Taguchi method, competitive manufacturing series. New York, 1990. pp. 7-80.

[60] H. Lei, D. Zhou, Y. Bao, Y. Li, Z. Han. Three-dimensional Improved Delayed Detached Eddy Simulation of a two-bladed vertical axis wind turbine. Energy Conversion and Management. 133 (2017) 235-48.